INSTITUT DE FRANCE
Académie des sciences

Comptes Rendus

Physique

Amélie Jarnac, Vincent L. R. Jacques, Laurent Cario, Etienne Janod, Steven L. Johnson, Sylvain Ravy and Claire Laulhé

Photoinduced charge density wave phase in 1T-TaS_2: growth and coarsening mechanisms

Volume 22, Special Issue S2 (2021), p. 139-160

Published online: 12 October 2021
Issue date: 3 December 2021

https://doi.org/10.5802/crphys.89

Part of Special Issue: Physics of ultra-fast phenomena
Guest editors: Éric Collet (Université Rennes 1, CNRS, France) and Sylvain Ravy (Université Paris-Saclay, CNRS, France)

Les Comptes Rendus. Physique *sont membres du Centre Mersenne pour l'édition scientifique ouverte*
www.centre-mersenne.org
e-ISSN : 1878-1535

Comptes Rendus
Physique
2021, 22, nº S2, p. 139-160
https://doi.org/10.5802/crphys.89

Physics of ultra-fast phenomena / *Physique des phénomènes ultra-rapides*

Photoinduced charge density wave phase in 1T-TaS_2: growth and coarsening mechanisms

Onde de densité de charge photoinduite dans 1T-TaS_2 : mécanismes de croissance et de mûrissement

Amélie Jarnac [a], Vincent L. R. Jacques [b], Laurent Cario [c], Etienne Janod [c], Steven L. Johnson [d], Sylvain Ravy [b] and Claire Laulhé [*, a]

[a] Université Paris-Saclay, Synchrotron Soleil, 91190, Saint-Aubin, France

[b] Université Paris-Saclay, CNRS, Laboratoire de Physique des Solides, 91405, Orsay, France

[c] Institut des Matériaux Jean Rouxel, Université de Nantes, CNRS, 2 rue de la Houssinière, 44322 Nantes Cedex 03, France

[d] Institute for Quantum Electronics, Eidgenossische Technishe Hochschule (ETH) Zürich, 8093 Zürich, Switzerland

Current address: Université Paris-Saclay, ONERA, DPHY, F-91123 Palaiseau, France (A. Jarnac)

E-mails: amelie.jarnac@onera.fr (A. Jarnac), vincent.jacques@u-psud.fr (V. L. R. Jacques), Laurent.Cario@cnrs-imn.fr (L. Cario), Etienne.Janod@cnrs-imn.fr (E. Janod), johnson@phys.ethz.ch (S. L. Johnson), sylvain.ravy@cnrs.fr (S. Ravy), claire.laulhe@synchrotron-soleil.fr (C. Laulhé)

Abstract. Recent experiments have shown that the high-temperature incommensurate (I) charge density wave (CDW) phase of 1T-TaS_2 can be photoinduced from the lower-temperature, nearly commensurate CDW state. In a first step, several independent regions exhibiting I-CDW phase modulations nucleate and grow. After coalescence, these regions form a multidomain I-CDW phase that undergoes coarsening dynamics, i.e. a progressive increase of the domain size or I-CDW correlation length. Using time-resolved X-ray diffraction, we show that the wave vector of the photoinduced I-CDW phase is shorter than in the I-CDW phase at equilibrium, and progressively increases towards its equilibrium value as the correlation length increases. We interpret this behaviour as a consequence of a self-doping of the photoinduced I-CDW, following the presence of trapped electrons in the vicinity of CDW dislocation sites. Putting together results of the present and past experiments, we develop a scenario in which the I-CDW dislocations are created during the coalescence of the I-CDW phase regions.

Résumé. Plusieurs expériences récentes ont montré que les impulsions laser dans les domaines optique ou proche infrarouge permettent de déclencher des transitions entre états à onde de densité de charge (ODC) dans 1T-TaS_2. Nous nous intéressons ici à la transition entre l'état à ODC presque commensurable (NC)

* Corresponding author.

et l'état à ODC incommensurable (I), habituellement observé au-dessus de 350 K. Lors de cette transition, plusieurs régions présentant les modulations de l'état I se forment et se développent. Lorsque la coalescence a lieu, ces régions se muent en domaines de la phase I photoinduite de 1T-TaS_2, caractérisés chacun par un phasage particulier de l'ODC I. La phase I ainsi fragmentée en domaines subit alors une dynamique de mûrissement, c'est-à-dire une augmentation progressive de la taille de domaine ou encore de la longueur de corrélation de l'ODC I. En utilisant la diffraction des rayons X résolue en temps, nous montrons que le vecteur d'onde de l'ODC I photoinduite est plus court que dans l'ODC I observée à l'équilibre thermodynamique. Celui-ci s'allonge progressivement vers sa valeur d'équilibre, en même temps que la longueur de corrélation de l'ODC I augmente. Nous attribuons ce comportement à un autodopage de l'ODC I photoinduite, dû à la présence d'électrons piégés au voisinage de dislocations de l'ODC I. En réalisant une synthèse des résultats des différentes expériences menées jusqu'à présent, nous développons un scénario dans lequel les dislocations de l'ODC I sont créées au moment de la coalescence.

Keywords. Photoinduced phase transitions, Pump–probe X-ray diffraction, Charge density wave compounds, Topological defects, Transition metal dichalcogenides.

Mots-clés. Transitions de phase photoinduites, Diffraction pompe–sonde des rayons X, Composés à onde de densité de charge, Défauts topologiques, Dichalcogénures de métaux de transition.

Available online 12th October 2021

1. Introduction

The physics of correlated materials involves couplings between charge, orbital, spin and lattice degrees of freedom, which give rise to a wealth of physical properties as well as complex phase diagrams [1, 2]. Correlated systems display equally fascinating out-of-equilibrium physics, in the form of ultra-fast symmetry changes known as photoinduced phase transitions [3–5], and occurrence of new emergent metastable or transient states with unexpected functionalities [6–11]. Charge density wave (CDW) phases are gapped phases that emerge at low temperatures, mostly in low-dimensional metals. They are characterized by a periodic modulation of both atomic positions and electron density [12]. A significant number of photoinduced phase transitions have been achieved in CDW compounds, most often corresponding to a *suppression* of the CDW order, i.e. a transition between a CDW state and a metallic state free of any structural modulation [13–27]. In layered CDW compounds such as rare-earth tritellurides and transition-metal dichalcogenides, photoinduced developments of CDW orders were also reported [28–37]. These photoinduced CDW orders were found to be either closely related to the ones observed at equilibrium [28–34] or genuinely new states of matter [35–37]. Their observation has highlighted an unforeseen complexity of the free energy surface of such layered materials, and the possibility of controlling transitions between several competing states by light.

In the last decade, it has been recognized that topological defects play a significant role in the photoinduced dynamics of CDW compounds [38]. In $LaTe_3$, the photoinduced suppression of CDW order was shown to be accompanied by a significant decrease of the CDW correlation length, which was attributed to the creation of CDW dislocations [25]. In 1T-TaS_2 at low temperatures, the metastability of the photoinduced "hidden" phase was shown to be due to the emergence of unpaired dislocations, which stabilize chiral domain patterns [36]. Here, we focus on the photoinduced phase transition between the nearly commensurate (NC) and the incommensurate (I) CDW states in 1T-TaS_2. The photoinduced I-CDW state (hereafter denoted I*-CDW) was revealed to be fragmented into nanometric domains that subsequently grow [32, 34]. It is established that this so-called phase-ordering process involves motion of topological defects of the I*-CDW: both domain wall motion [32] and dislocation annihilation [34] were evoked.

1T-TaS_2 is formed by sheets of edge-linked TaS_6 octahedra (Figure 1a) [39]. In the high-symmetry phase ($T > 543$ K), Ta-atoms form a regular hexagonal lattice within a layer. As temperature decreases, three CDW phases stabilize alternately [40, 41], namely the incommensurate (I), nearly-commensurate (NC) and commensurate (C) phases. The first transition to

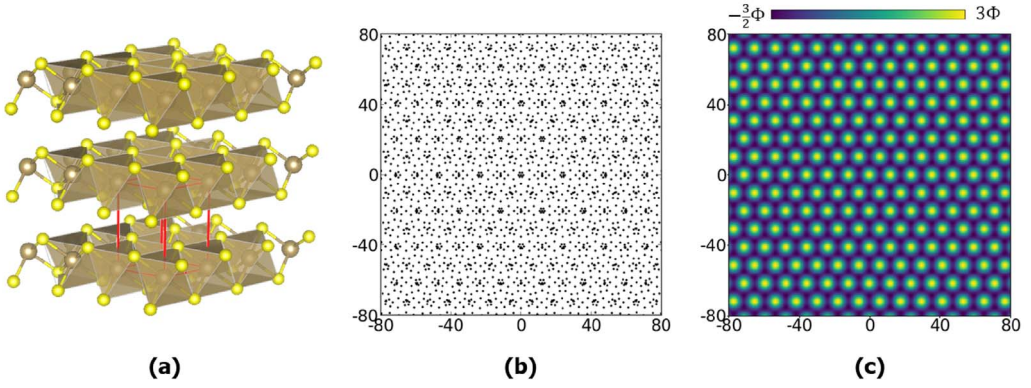

Figure 1. (a) Crystal structure of 1T-TaS_2 [44]. The hexagonal unit-cell is represented in red. (b,c) Ta-plane located at $z = 0$. All the length-scales are in Å. (b) Ta-plane exhibiting modulations of the I phase (350 K < T < 543 K). The Ta-atoms are represented as black dots, their displacements being exaggerated for visualization purposes. (c) Spatial dependence of the I-CDW real order parameter $\alpha(\vec{r}) = \Phi \sum_{j=1}^{3} \cos(\vec{q_I^j} \cdot \vec{r} + \theta_I^j)$, which corresponds to the charge density modulation.

the I-CDW phase occurs below 543 K and is believed to be driven by Fermi surface nesting [42], similarly to the Peierls distortion in one-dimensional systems [12]. The I-CDW phase is a triple-q modulated phase, characterized by the wave vectors $\vec{q_I^1} \approx 0.283\vec{a}^* + (1/3)\vec{c}^*$ and equivalents by 3-fold symmetry (Figure 2a). An atom which lies at a position $\vec{r}$ of the hexagonal lattice in the high temperature phase gets displaced in the I-CDW phase by $\vec{u}(\vec{r}) = \sum_{j=1}^{3} u_I \vec{e}_j \sin(\vec{q_I^j} \cdot \vec{r} + \theta_I^j)$, where $\vec{e}_j$ and θ_I^j are the polarisation and the phase associated with the j^e structural modulation. The amplitude u_I is the same for all three modulation components. The modulated Ta-positions observed in the I-CDW phase of 1T-TaS_2 are represented in Figure 1b. The electronic charge density is also modulated, and written in the form $\rho(\vec{r}) = \rho_0[1 + \alpha(\vec{r})]$, where ρ_0 is the density of conduction electrons and $\alpha(\vec{r}) = \Phi \sum_{j=1}^{3} \cos(\vec{q_I^j} \cdot \vec{r} + \theta_I^j)$ the order parameter of the I-CDW phase, Φ denoting the amplitude of each of the 3 electronic density modulations (Figure 1c) [43]. Note that the three θ_I^j phases may be different, however their sum has to be a multiple of 2π in order to yield peaks in the electron density as observed experimentally [43]. Below 350 K, the modulation wave vectors suddenly rotate by about 12° in the $(\vec{a}^*, \vec{b}^*)$ plane, marking the onset of the NC-CDW state (Figure 2a). At 300 K, the NC phase exhibits modulation vectors $\vec{q_{NC}^1} = 0.245\vec{a}^* + 0.068\vec{b}^* + (1/3)\vec{c}^*$ and equivalents by 3-fold symmetry. The in-plane components of $\vec{q_{NC}^1}$ are close to the commensurate values $(3/13)\vec{a}^* + (1/13)\vec{b}^*$. This commensurate, triple-q in-plane modulation is actually achieved below 180 K in the C-CDW phase.

X-ray diffraction is a perfectly suited method to study the structural evolution of CDWs, thanks to the selectivity and high-resolution in q-space it provides. More specifically: (1) A structural modulation with wave vector $\vec{q}$ gives rise to satellite peaks located at positions $\pm\vec{q}$ with respect to each Bragg peak of the unmodulated lattice (Figure 2a). (2) The integrated intensity of a CDW satellite peak is proportional to both the average of the square of the structural modulation amplitude and the volume fraction of the CDW phase in the sample. (3) After deconvolution of the instrument profile, the width of a CDW satellite peak is inversely proportional to the CDW correlation length. In the case of 1T-TaS_2, previous time-resolved diffraction studies have shown that the photoinduced I*-CDW phase appears within a picosecond after laser excitation [30] through a nucleation and growth process [32,33]. The correlation length of the newly formed I*-CDW phase,

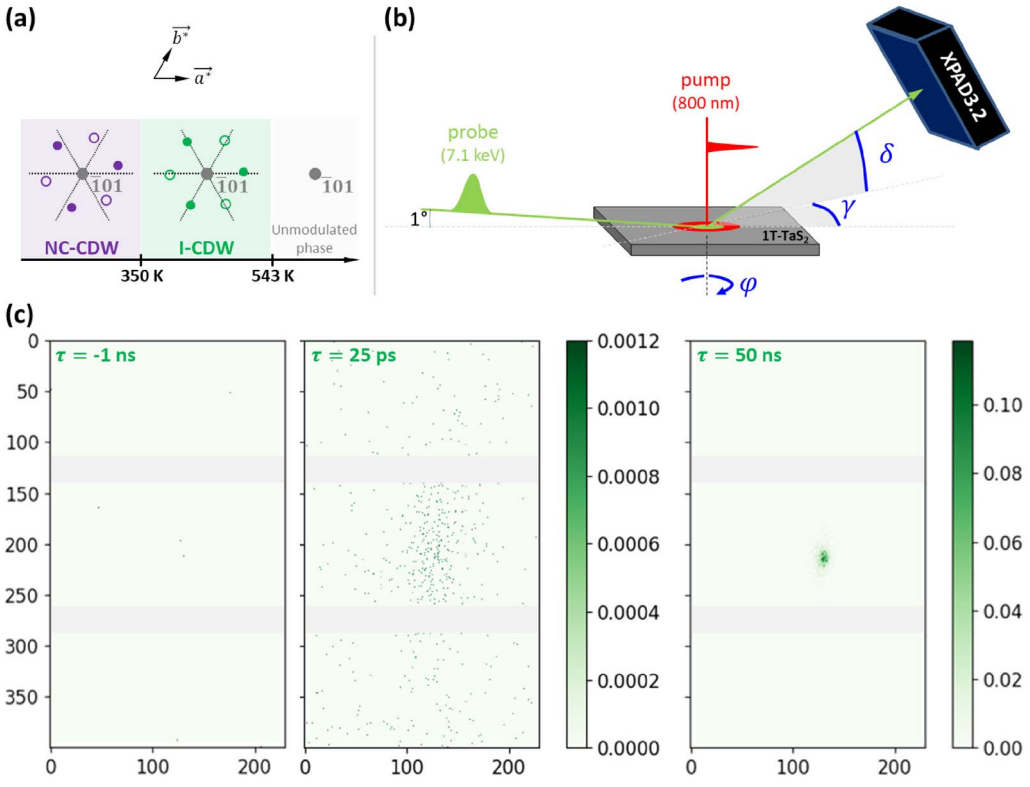

Figure 2. (a) Schematic representation of diffracted intensity in reciprocal space, as a projection in the $(\vec{a}^*, \vec{b}^*)$ plane of 1T-TaS_2. Satellite peaks related to the $\bar{1}01$ lattice peak are represented in purple for the NC phase and in green for the I phase. Their coordinate along c^*-axis can take two possible values: $1 + (1/3)$ (filled circles) and $1 - (1/3)$ (open circles). (b) Experimental setup and definition of the angles φ (sample rotation), δ and γ (detector rotations). (c) Diffracted intensity measured in the vicinity of the reciprocal space position $\bar{1}01 - \vec{q}_I^1$ for various pump–probe delays τ (265 K, absorbed fluence 3.9 mJ/cm^2). These images were obtained by summing diffracted intensities over a 1.75° φ-range. The image axes are graduated in pixel units, the pixel size being 135 µm. The non-sensitive regions of the detector are represented in light grey. The diffracted intensity is color-coded according to the scales displayed at the right of each image (in counts/s).

initially limited to a few nanometres, subsequently increases on timescales ranging from few tens of picoseconds to nanoseconds [32–34]. At this stage, considering together the time evolutions of both the I*-CDW correlation lengths and the volume fraction of the I*-CDW phase is crucial to distinguish between two very different phase development processes: *growth* and *phase ordering*. The *growth* of isolated I*-CDW phase regions from nuclei of the I*-CDW phase is characterized by a concomitant increase of the volume fraction of the I*-CDW phase and of the I*-CDW correlations lengths. After coalescence of the I*-CDW phase regions, a short-range correlated I*-CDW phase is observed in a single region of the sample. The I*-CDW *phase ordering* (or coarsening) that takes place afterwards corresponds to an increase of the I*-CDW correlation length in a constant volume fraction of the I*-CDW phase.

In the following, we present a new data set showing the development of a I*-CDW satellite in 1T-TaS_2 after laser excitation at 800 nm wavelength (Section 3). Based on a joint analysis of

the I*-CDW satellite peak profile and integrated intensity, we give evidence for a coarsening process in the $(\vec{a},\vec{b})$ plane (Section 3.1). For the first time in this coarsening regime, the wave vector of the photoinduced I*-CDW phase $\vec{q}_I^*$ could be tracked as the I*-CDW correlation length increases. We show that the in-plane component of $\vec{q}_I^*$ is initially shorter than in the I-CDW phase at equilibrium, and gradually increases towards its equilibrium value as the correlation length increases (Section 3.2). In Section 4, we discuss the possible scenarios behind this observation, in the framework of self-hole doping by CDW dislocations.

2. Experimental setup and method

The pump–probe time-resolved diffraction experiment took place at the CRISTAL beamline of SOLEIL synchrotron source (Saint Aubin, France). The sample was a platelet-like, (001)-oriented single crystal of 1T-TaS_2, few hundreds of micrometers thick and synthesised as described in Ref. [45].

The NC → I phase transition was triggered by 40 fs, 800 nm laser pulses at normal incidence with respect to the (001) surface plane. The laser fluence, which was calculated as the ratio between the energy of a single laser pulse and the full width half maximum (FWHM) of the laser beam, amounted 6.7 ± 0.8 mJ/cm^2. Given the reflectivity of the sample at 800 nm ($R = 0.417$ [46]), only 58.3% of this laser fluence i.e. 3.9 ± 0.5 mJ/cm^2 was actually absorbed.

The growth of the photoinduced I*-CDW phase was probed by X-ray diffraction at various delays τ after laser excitation, using 7.1 keV, 12 ps X-ray pulses. This relatively short pulse duration was provided during the low-α operation of the storage ring [47]. Intensity decays of the laser pump and X-ray probe beams are described by very different values of penetration depths in 1T-TaS_2: $\delta_X = 7.42$ µm [48] and $\delta_L \approx 30$ nm,[1] respectively. The incidence angle of the X-ray pulses was fixed to 1° with respect to the (001) surface plane, in order to limit the effective penetration depth of the probe to 130 nm and thereby minimize background signal from unpumped regions. The diffraction condition was tuned by rotating the sample about its surface normal, by an angle hereafter denoted φ. The diffraction signal was recorded with the 2D gateable detector XPAD3.2 [49], which can be rotated through both an elevation angle δ and an azimuthal angle γ (Figure 2b).

Determining the time-evolution of the wave vector of the photoinduced I*-CDW requires a very high resolution in reciprocal space. A resolution of about 6×10^{-4} Å^{-1} could be achieved by: (1) using a Si(111)-monochromator ($\Delta E/E = 2.4 \times 10^{-4}$) in conjunction with the low-divergent synchrotron source and (2) setting a relatively long sample-to-detector distance of 82.8 cm, leading to a correspondence of 0.009°/pixel.

At 1° incidence, the X-ray beam footprint on the sample was 1.7 mm × 0.5 mm FWHM. The laser spot on the sample was set to twice that size, i.e. 3.5 mm × 1.0 mm FWHM. The diffraction signals were recorded in a regular pump–probe scheme. The laser pulses were electronically phase-locked to a single electron bunch of the storage ring, using TimBeL boards [50] and an in-phase/quadrature modulator. A repetition rate of 500 Hz was chosen in order to ensure a complete disappearance of the photoinduced I*-CDW phase before the arrival of the following laser pulse, allowing cumulative measurement of the pump–probe cycles. A significant number of scans were performed at negative delays close to the I*-CDW satellite peak position, regularly throughout the experiment, in order to check that no residual I*-CDW peak would form as the number of pump–probe cycles increased.

[1] Both the reflectivity R and the penetration depth δ_L of 800 nm photons in 1T-TaS_2 were calculated from the complex optical index, which itself was deduced from the real and imaginary parts of the dielectric function published in [46].

The sample temperature was regulated by means of a N_2 blower. Cryostats of this type have a limited cooling power, so that the controller temperature and the actual sample temperature may differ, especially in the present case of a laser-heated, millimetric sample. We estimate the actual sample temperature to be about 25 K higher than the controlled temperature, as I-CDW satellite peaks become observable at negative pump–probe delays for temperature setpoints higher than 325 K. The data presented in this article were acquired for a controlled temperature of 265 K.

3. Results

We first demonstrate the occurrence of a photoinduced NC → I phase transition in the chosen experimental conditions (absorbed fluence: 3.9 mJ/cm^2, controller temperature: 265 K). Figure 2c presents images of the diffracted intensity summed over a 1.75° wide φ-range around the I-CDW satellite peak position $\bar{1}01 - \vec{q}_I^1$, for three delays before and after laser excitation. No contribution is observed before laser excitation, which is expected since the sample lies in its NC-CDW phase. Shortly after laser excitation (τ = 25 ps), a diffuse scattering signal appears in the vicinity of the I-CDW satellite peak position, which shows the onset of the photo-induced I* phase. This scattering progressively narrows over time and eventually forms a well-defined diffraction peak at longer delays (τ = 50 ns). These observations are consistent with those previously reported in Refs. [16,30,32–34].

Figure 3 shows the I*-CDW satellite peak profiles as functions of the angles φ, δ and γ, for various delays after laser excitation. The diffracted intensities displayed on the φ-profiles correspond to photon counts summed over the detector area presented in Figure 2c. The δ- and γ-profiles were obtained by first summing all the images taken along a φ-scan, and then projecting photon counts along the horizontal and vertical directions of the detector respectively, assuming a correspondence of 0.009°/pixel.

3.1. *Development of the I*-CDW phase*

The CDW correlation lengths correspond to distances over which both the amplitude and the phase of the CDW are homogeneous. As such, they are of central importance for discussing the CDW growth and phase-ordering processes. It has been emphasized that determining the 3D profile of a CDW satellite peak in reciprocal space allows retrieval of the CDW correlation lengths in all directions of space [33]. In the following, we provide an estimation of the correlation lengths of the I*-CDW, both in the $(\vec{a},\vec{b})$ plane and along $\vec{c}$. Those are hereafter denoted $\xi_{a,b}$ and ξ_c.

We first determined the time-dependent FWHMs of the I*-CDW satellite peak, $\Delta\delta(\tau)$ and $\Delta\gamma(\tau)$, by fitting pseudo-Voigt functions to the profiles along δ and γ, respectively (Figure 3). The contributions of instrumental resolution and sample mosaicity were then removed from the measured satellite peak widths, according to the following expressions: $\Delta\delta'(\tau) = \sqrt{[\Delta\delta(\tau)]^2 - [\Delta\delta_B]^2}$ and $\Delta\gamma'(\tau) = \sqrt{[\Delta\gamma(\tau)]^2 - [\Delta\gamma_B]^2}$. The angular widths $\Delta\delta_B = 0.075°$ and $\Delta\gamma_B = 0.043°$ correspond to those of the nearest Bragg peak $\bar{1}01$. The correlation lengths $\xi_{a,b}$ and ξ_c were finally estimated by using the following equations:

$$\xi_{a,b}(\tau) = \frac{2\pi}{\Delta q_{a^*,b^*}} = \frac{\lambda_X}{2\tan\left[\frac{\Delta\gamma'(\tau)}{2}\right]\cos[\delta(\tau)]} \tag{1}$$

$$\xi_c(\tau) = \frac{2\pi}{\Delta q_{c^*}} = \frac{\lambda_X}{2\tan\left[\frac{\Delta\delta'(\tau)}{2}\right]\cos[\delta(\tau)]}, \tag{2}$$

where λ_X is the X-ray wavelength. $\Delta q_{a^*,b^*}$ and Δq_{c^*} are the FWHMs of the I*-CDW satellite peak in reciprocal space related to the limited I*-CDW correlation lengths (Figure 4).

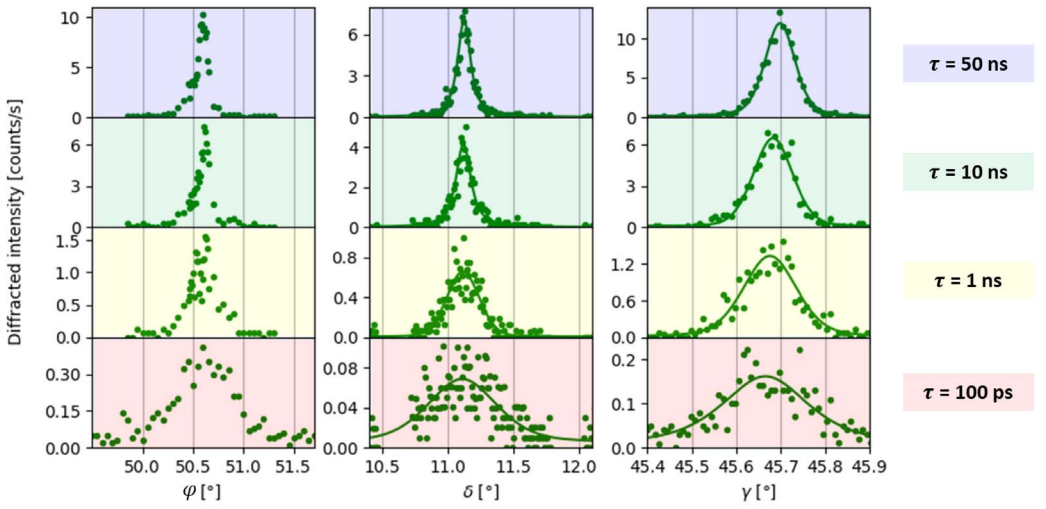

Figure 3. Profiles of the $\bar{1}01-\vec{q}_{I*}^{\bar{1}}$ I*-CDW satellite peak as functions of the angles φ, δ and γ, for selected pump–probe delays (265 K, absorbed fluence 3.9 mJ/cm^2). The dots represent measured data and the solid lines their best fit using a pseudo-Voigt function. Those fits allow extracting the peak widths and angular positions as a function of the pump–probe delay τ.

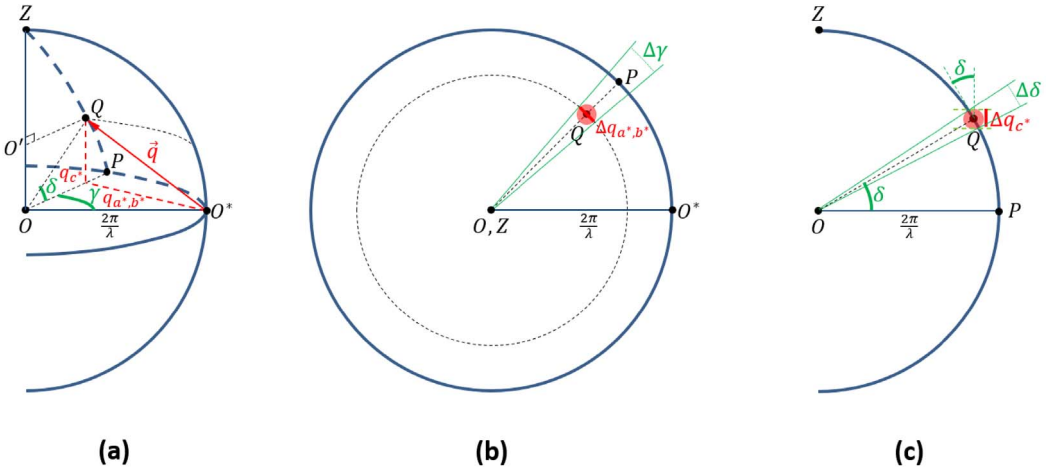

Figure 4. (a) 3D-view of the Ewald's sphere, with the I*-CDW satellite peak fulfilling the diffraction condition. The scattering vector $\vec{q} = -\vec{a}^* + \vec{c}^* - \vec{q}_{I*}^{\bar{1}}$ intercepts the Ewald sphere at point Q. (b) Orthogonal projection in the (OO^*P) plane, which allows defining $\Delta q_{a^*,b^*}$ (red line segment). (c) Orthogonal projection in the (OPQ) plane, which allows defining Δq_{c^*} (red line segment). Note that for ease of calculation, the X-ray incidence angle has been approximated to 0 (instead of 1°), i.e. $\vec{c}^*$ is supposed to lie along the OZ direction.

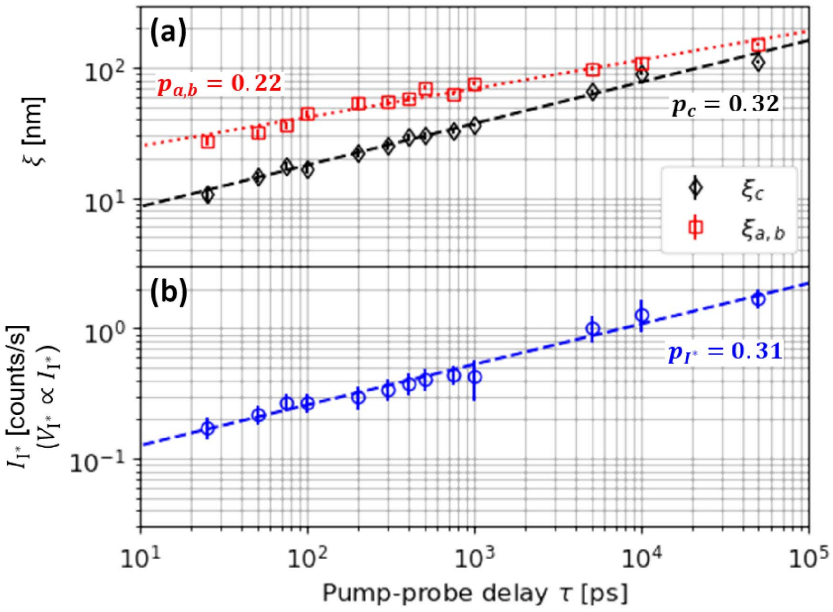

Figure 5. (a) Time-evolution of the I*-CDW correlation lengths, in the $(\vec{a}, \vec{b})$ plane ($\xi_{a,b}$, open squares) and along $\vec{c}$ (ξ_c, open diamonds). (b) Integrated intensity of the $\bar{1}01 - \vec{q}_{I^*}^{\vec{1}}$ satellite peak of the I*-CDW, I_{I^*}. The error bars correspond to $\pm\sigma$ where σ is the standard deviation. Those were determined by propagating the errors on $\Delta\delta(\tau)$ and $\Delta\gamma(\tau)$, which themselves were estimated from the I* satellite peak fitting. Dotted lines mark the best fits of the data using the power-law function $A \times \tau^p$. The optimized values of p are indicated in the figure. The temperature setpoint was 265 K and the absorbed fluence 3.9 mJ/cm^2.

The time-dependent correlation lengths $\xi_{a,b}(\tau)$ and $\xi_c(\tau)$ do not exceed few tens of nm in the pump–probe delay range studied (Figure 5a). Those exhibit a linear behaviour when plotted on a double logarithmic scale, which implies that they exhibit a power-law dependence on time $\xi \propto \tau^p$. Two distinct exponents p are found for $\xi_{a,b}$ and ξ_c: $p_{a,b} = 0.22 \pm 0.04$ and $p_c = 0.32 \pm 0.03$, respectively. The correlation lengths $\xi_{a,b}$ and ξ_c correspond to distances over which the phases $\theta_{I^*}^j$ of the I*-CDW are homogeneous. As a consequence, the observed increase of the I*-CDW correlation lengths stems either from an expansion of regions exhibiting homogeneous CDW-phases $\theta_{I^*}^j$ (growth, Figure 6a), or from a homogenization of the CDW-phases $\theta_{I^*}^j$ within a single region exhibiting I*-CDW order (ordering, Figure 6b). The latter two processes can be distinguished by determining the time-dependence of the volume fraction of the I*-CDW phase, V_{I^*}.[2]

The integrated intensity of the I*-CDW satellite peak I_{I^*} is directly proportional to V_{I^*}. However, it is also directly proportional to the square of the average I*-CDW amplitude Φ_{I^*}. The amplitude Φ_{I^*} increases concomitantly with the I*-CDW gap formed at the Fermi level [42]. Although the latter quantity has never been probed following the photoinduced NC → I phase transition in 1T-TaS_2, pump–probe photoemission experiments have allowed establishing that the typical timescales of formation or recovery of CDW gaps lie below few ps [20, 25, 51–53]. Interestingly,

[2] In this work, the volume fraction of the I*-CDW phase is to be understood as the total volume of the I*-CDW phase region(s) divided by the volume probed by X-rays.

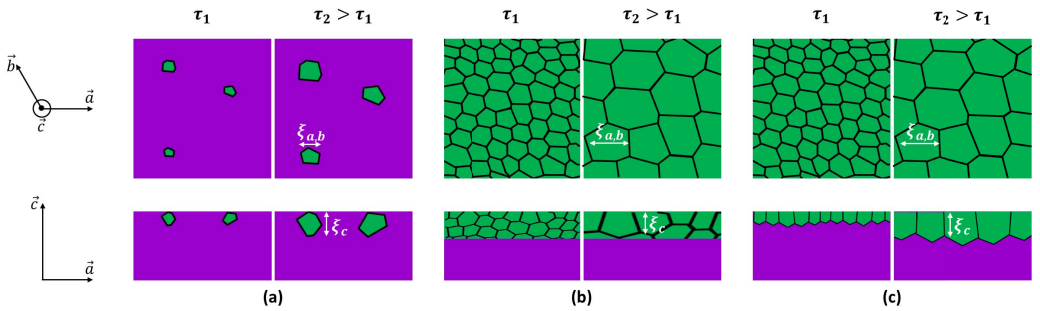

Figure 6. Schematic representation of the three scenarios that have been reported for the development of the I*-CDW phase (times after laser excitation: τ_1 and $\tau_2 > \tau_1$). The top and bottom rows show views of the 1T-TaS_2 crystal along its c-axis and along a direction normal to the c-axis, respectively. (a) Growth of isolated I*-CDW phase regions. In this case, the volume of the I*-CDW phase is directly proportional to ${\xi_{a,b}}^2 \times \xi_c$ [33]. (b) Coarsening of I*-CDW domains in a large I*-CDW region. In this case, the volume of the I*-CDW phase is constant [32]. (c) Growth of the I*-CDW phase region along $\vec{c}$, and domain coarsening in the $(\vec{a}, \vec{b})$ plane. In this case, the volume of the I*-CDW phase is directly proportional to ξ_c [present work].

a previous ultrafast electron diffraction study unveiled two characteristic time scales of the photoinduced NC → I phase transition in 1T-TaS_2 [30] (pump wavelength 775 nm). The first characteristic time scale, of 1.5 ps, was attributed to the nucleation of the I* phase, i.e. the increase of Φ_{I^*} towards its equilibrium value in finite regions of the sample. The second characteristic time scale, of few tens of ps, was attributed to the growth of the I* phase nucleated regions. Given these results, it is reasonable to assume that in the delay range $\tau \geq 25$ ps investigated in this work, Φ_{I^*} has reached its maximum value throughout the I*-CDW regions. Under the latter hypothesis, the volume fraction of the I*-CDW phase can be directly inferred from the integrated intensity of the I*-CDW satellite peak, using $V_{I^*} \propto I_{I^*}$. The dependence of V_{I^*} on pump–probe delay is given in Figure 5b, on a double logarithmic scale. It keeps increasing in the (0–50 ns) delay range investigated, following a power-law scaling $V_{I^*} \propto \tau^{0.31}$, which indicates a continuous expansion of the volume fraction of the I*-CDW phase in the sample. The scenario of a pure phase-ordering process, in which the correlation length increases in a fixed volume fraction of the I*-CDW phase (Figure 6b), is thus very unlikely. In the case where I*-CDW regions would grow without being in contact (Figure 6a), we expect the integrated intensity of the I*-CDW satellite peak to be proportional to ${\xi_{a,b}}^2 \times \xi_c$ and, therefore, to τ^{p_g} with $p_g = 2 \times p_{a,b} + p_c = 0.8 \pm 0.1$. This exponent is inconsistent with our findings ($p_{I^*} = 0.31 \pm 0.02$). We conclude that none of the scenarios depicted in Figures 6a,b matches with the experimental observations. A model thus has to be built, where (1) both the I*-CDW correlation lengths and the volume fraction of the I*-CDW phase increase, and (2) the correlated volume and the volume fraction of the I*-CDW phase grow at different rates. Noticing that V_{I^*} and ξ_c have the same time-dependence ($p_{I^*} \approx p_c$), we propose that the I*-CDW phase is developed in a layer of thickness $\xi_c(\tau)$ at the surface of the sample. The volume fraction of the I*-CDW phase then grows concomitantly with ξ_c, according to the power-law function τ^{p_c}. On the other hand, one can assume that the I*-CDW phase has already developed over the entire $(\vec{a}, \vec{b})$ plane. It is divided into domains exhibiting each a different set of CDW-phases $\theta^j_{I^*}$, and undergoes coarsening along the $\vec{a}$ and $\vec{b}$ directions (Figure 6c). We exclude the possibility that isolated regions of the I*-CDW phase, growing at a rate $\tau^{p_{I^*}}$, would host several CDW-phase domains growing at a rate τ^{p_g}. Indeed, previous experiments have shown that

before coalescence, both the nucleated I*-CDW phase regions and the correlated volume grow at the same rate [33], thereby establishing that the CDW-phases are homogeneous within isolated I*-CDW regions. Finally, let us note that if our experiment shows a proportionality between the c-axis correlation length and the volume fraction of the I* phase, this does not necessarily mean that the thickness of the I* phase is equal to the time-dependent $\xi_c(\tau)$ correlation length (Figure 6c). Namely, a scenario where the ξ_c correlation length would be a fixed fraction of the thickness of the I*-CDW layer cannot be excluded. We however consider it unlikely, as it would imply that coarsening and growth along the c-axis, which are markedly different processes, happen at the same rate.

It is interesting to discuss the proposed scenario (Figure 6c) in the framework of the previous findings of Haupt *et al.* [30]: they report that the time needed to achieve a complete transition to the I-CDW phase over a 22 nm thick 1T-TaS_2 sample decreases from ~500 ps to ~200 ps as the incident fluence increases from 1.3 mJ/cm^2 to 2.1 mJ/cm^2. In our experiment, the sample is much thicker than the laser penetration depth, so that we cannot expect a development of the I phase over the whole sample. Nevertheless, it is possible to estimate the time needed for the I* phase to get fully developed across a 20 nm thickness of our 1T-TaS_2 sample, $\tau_{20\,\mathrm{nm}}$. Assuming the scenario depicted in Figure 6c, $\tau_{20\,\mathrm{nm}}$ simply corresponds to the delay at which ξ_c reaches 20 nm, that is $\tau_{20\,\mathrm{nm}} = 140$ ps (Figure 5b). The latter delay is consistent with the ones reported by Haupt *et al.*, given the incident fluence used in the present work (6.7 ± 0.8 mJ/cm^2).

3.2. *Time evolution of the I*-CDW wave vector*

The defect structures that lead to short range correlated CDW states can modify both the spatial distribution of electrons and the density of states [54] and, in turn, the wave vectors of the I*-CDW phase $\vec{q}^{\,j}_{I^*}$. In the following, we give evidence for a progressive increase of the $(\vec{a}^*, \vec{b}^*)$-plane component of $\vec{q}^{\,1}_{I^*}$ towards its equilibrium value, which we will relate to CDW dislocation annihilation processes in Section 4.

The wave vector of the photoinduced I*-CDW at time τ, $\vec{q}^{\,1}_{I^*}(\tau)$, has coordinates $(h_{I^*}(\tau) - h_B, k_{I^*}(\tau) - k_B, l_{I^*}(\tau) - l_B)$ in the time-dependent basis $(\vec{a}^*(\tau), \vec{b}^*(\tau), \vec{c}^*(\tau))$ of the reciprocal space, where $(h_{I^*}(\tau), k_{I^*}(\tau), l_{I^*}(\tau))$ are the coordinates of a satellite peak and (h_B, k_B, l_B) those of the corresponding lattice peak. In order to study the dynamics of $\vec{q}^{\,1}_{I^*}(\tau)$, one has thus to determine the time-evolution of both the reciprocal lattice vectors and the $(h_{I^*}(\tau), k_{I^*}(\tau), l_{I^*}(\tau))$ coordinates.

3.2.1. *Time evolution of the underlying crystal lattice*

Assuming that the lattice remains hexagonal at all times after laser excitation, the set of vectors $(\vec{a}^*(\tau), \vec{b}^*(\tau), \vec{c}^*(\tau))$ can be entirely determined from the orientation matrix of the crystal (3 rotation parameters) and the values of the a and c cell parameters. We evaluated the latter 5 parameters for all the pump–probe delays investigated, by using the GHKL computation library [55] along with the angular positions of both $\bar{1}01$ and $\bar{1}02$ Bragg peaks.

The experimental values of the angles $\varphi(\tau)$, $\delta(\tau)$ and $\gamma(\tau)$ were determined as the first moments of the normalized intensity distributions, which are partly shown in Figure 7. One can observe that the angular positions of the $\bar{1}01$ and $\bar{1}02$ Bragg peaks exhibit similar time evolutions (Figure 8a). The peak angles $\varphi(\tau)$ and $\delta(\tau)$ increase and decrease, respectively, by a few hundredth of degrees within 50 ps. Both angles then remain constant up to 1 ns, and progressively recover their initial values in the τ-range (1–50 ns). The angle $\gamma(\tau)$ does not exhibit any significant changes throughout the whole pump–probe cycle. The orientation matrix calculated from the angular positions of the two lattice reflections $\bar{1}01$ and $\bar{1}02$ is found to be constant over time.

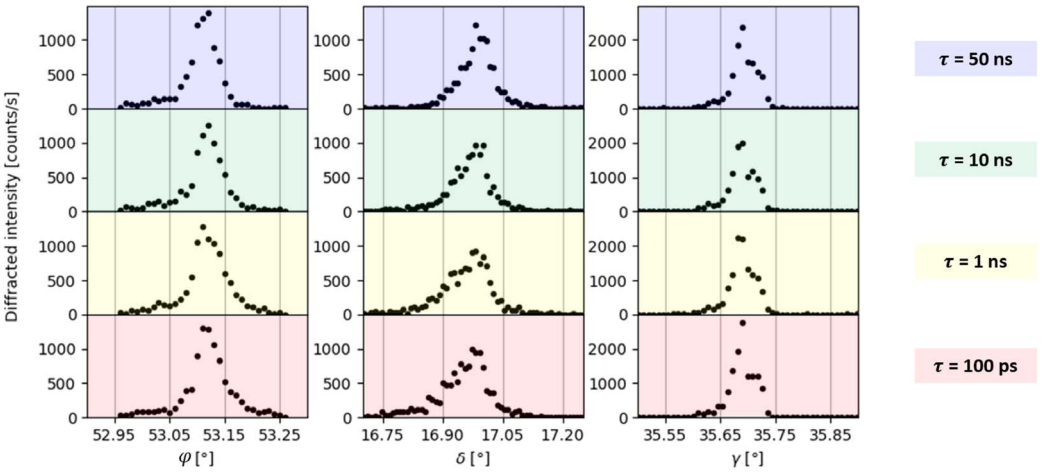

Figure 7. Profiles of the $\bar{1}01$ lattice peak as functions of the angles φ, δ and γ, for selected pump–probe delays (265 K, absorbed fluence 3.9 mJ/cm^2).

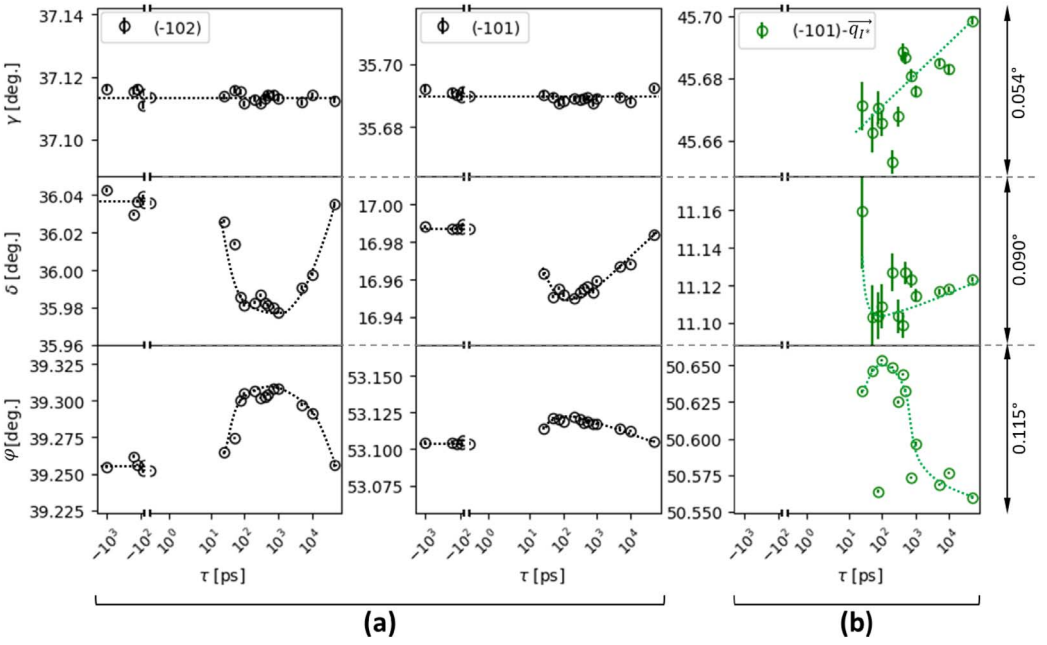

Figure 8. Time-evolution of the angles φ, δ and γ for the $\bar{1}01$ and the $\bar{1}02$ lattice peaks (a), and for the $\bar{1}01 - \vec{q}^{\bar{1}}_{I^*}$ satellite peak (b). The error bars correspond to $\pm\sigma$ where σ is the standard deviation. Those take into account the accuracy of the diffractometer (0.001°) as well as the propagation of statistical errors when determining the first moments of the intensity distributions (φ angle values and (a) panel). The error bars presented in panel (b) for δ and γ angles were calculated using the accuracy of the diffractometer and the errors estimated from the I* satellite peak fitting. The dotted lines are guides for the eye. The temperature setpoint was 265 K and the absorbed fluence 3.9 mJ/cm^2.

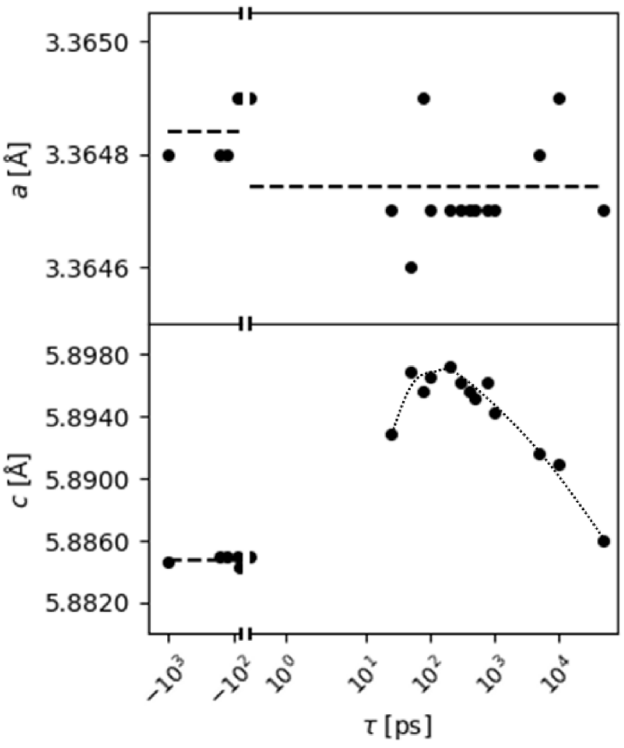

Figure 9. Time-evolution of the cell parameters a and c, as determined by using the GHKL library with the measured diffraction angles of the $\bar{1}01$ and the $\bar{1}02$ lattice peaks. The dashed lines indicate averaged values of the a and c parameters before laser excitation ($\tau < 0$), as well as the averaged value of a after laser excitation ($\tau > 0$). The dotted line is a guide for the eye. The base temperature was 265 K and the absorbed fluence 3.9 mJ/cm^2.

The time-dependent cell parameters deduced from measurements on the $\bar{1}01$ Bragg peak are reported in Figure 9. The shifts of $\varphi(\tau)$ and $\delta(\tau)$ mentioned above appear to be due to a transient lattice expansion along the c-axis, i.e. in the direction perpendicular to the sample's surface. This phenomenon is generally observed in laser-excited solids and stems from the propagation of a laser-induced strain wave [56]. A very small contraction of the lattice in the $(\vec{a}, \vec{b})$ plane could also be detected after laser excitation ($\langle \Delta a/a \rangle = -3 \times 10^{-5}$), which can be attributed to longitudinal-to-transverse strain coupling (Poisson effect) [57].

3.2.2. *Dynamics of the I*-CDW satellite peak*

The orientation matrices and cell parameters being known for all pump–probe delays, we now turn to the determination of the time-dependent coordinates of the forming I*-CDW satellite peak $(h_{I^*}(\tau), k_{I^*}(\tau), l_{I^*}(\tau))$. The $\varphi(\tau)$ angular positions of the I*-CDW satellite peak were determined from the calculation of the first moments of the diffraction profiles, as was done for the $\bar{1}01$ and $\bar{1}02$ Bragg peaks. The same method could not be safely used to extract the $\delta(\tau)$ and $\gamma(\tau)$ values, as part of the satellite peak intensity falls into dead-zones of the detector (Figure 2). We thus determined those latter two angles by fitting a pseudo-Voigt function to the respective diffraction profiles (Figure 3). Figure 8b shows the time-evolution of the $\varphi(\tau)$, $\delta(\tau)$ and $\gamma(\tau)$ angles of the I* satellite peak. The data are noisier than those related to the lattice peaks (Figure 8a), despite the

fact that we adapted the total counting times to get sufficient statistics on the I* satellite peak intensities. This indicates drifts in some of the experimental parameters over the 33 hour period during which we acquired the series of measurements on the time-dependence of the I* satellite peak. The time-dependence of the $\delta(\tau)$ angle of the I*-CDW satellite peak is found to exhibit qualitatively the same features as the ones measured for the lattice peaks. On the other hand, time evolutions of the $\varphi(\tau)$ and $\gamma(\tau)$ angles differ significantly for the lattice and satellite peaks. The $\varphi(\tau)$ angle of the I* satellite peak is found to increase in the first 50 ps, as for the lattice peaks. However, its subsequent decrease is about ten times faster. Moreover, in marked contrast with the constant $\gamma(\tau)$ angle observed for lattice peaks, we report a continuous increase of the $\gamma(\tau)$ angle of the I*-CDW satellite peak over time. Hence, we give evidence for distinct dynamics of the satellite and lattice diffraction peaks, which in turn indicates a *time-dependence* of the I*-CDW wave vector $\vec{q}_{I^*}^{\,\parallel}$.

The time-dependent coordinates of the forming I*-CDW satellite peak $(h_{I^*}(\tau), k_{I^*}(\tau), l_{I^*}(\tau))$ were calculated by using the GHKL library [55] and the previously determined time-dependent basis of the reciprocal space, $(\vec{a}^*(\tau), \vec{b}^*(\tau), \vec{c}^*(\tau))$. The coordinates of $\vec{q}_{I^*}^{\,\parallel}$ were then deduced from $(h_{I^*}(\tau), k_{I^*}(\tau), l_{I^*}(\tau))$, by subtracting the coordinates of the nearest lattice peak $\bar{1}01$. The CDW wave vectors of 1T-TaS_2 are usually divided into two components, $q_{\mathrm{CDW}}^{\perp}\vec{}$ and $q_{\mathrm{CDW}}^{\parallel}\vec{}$ (Figure 10a). The c^*-axis component of the CDW wave vector $q_{\mathrm{CDW}}^{\perp}\vec{}$ is related to the stacking of the 2D-CDWs from one layer to the other. In both the I and NC phases of 1T-TaS_2, it is determined by interlayer Coulombic interactions which yield a $3c$ stacking period and $\|q_{\mathrm{CDW}}^{\perp}\vec{}\| = 1/3$ [58,59]. The $(\vec{a}^*, \vec{b}^*)$-plane component $q_{\mathrm{CDW}}^{\parallel}\vec{}$ determines both the period and the orientation of the 2D hexagonal lattices of charge modulation. The time-dependences of the polar coordinates of $\vec{q}_{I^*}^{\,\parallel}$, $q_{I^*}^{\parallel}$ and α_{I^*}, are represented in Figures 10b and c respectively (black circles). The coordinates $q_I^{\parallel}$ and α_I of the I-CDW wave vector measured at equilibrium (385 K, no laser excitation) are also reported for comparison purposes (red dotted lines). The values of $q_I^{\parallel}$ and α_I found for the I-CDW at equilibrium are in agreement with previous reports [40,59–61]. We find that the I-CDW develops in the $(\vec{a}, \vec{b})$ plane with a wave vector component $q_I^{\parallel} = 0.2827(1)$. Structural modulations in the $(\vec{a}, \vec{b})$ plane are observed in directions slightly off the main hexagonal axes. We find an angle α_I of 0.1(2)°, which falls in the range of previously reported values: 0° [59,60], 0.38(2)° [40] and 1° [61]. The large dispersion of α_I values reported so far indicates that the I-CDW tilt angle might be sample-dependent. At the onset of the I*-CDW formation ($\tau = 25$ ps), $q_{I^*}^{\parallel}$ is found 0.3% smaller than $q_I^{\parallel}$ (Figure 10b). The orientation of the in-plane I*-CDW modulation with respect to the hexagonal axes also differs from the one observed in the I phase at equilibrium (Figure 10c). Both parameters $q_{I^*}^{\parallel}$ and α_{I^*} evolve in time to reach their reference values, albeit on different timescales: few tens of ns for $q_{I^*}^{\parallel}$, about 1 ns for α_{I^*}).

Let us note that due the limited penetration depth of the 800 nm photons in 1T-TaS_2 ($\delta_L \approx$ 30 nm, see Section 2) and the resulting inhomogeneous excitation profile, it is expected that the cell parameters a and c exhibit a significant depth-dependence over the 130 nm probed region. The values of a and c given in Figure 9, which are deduced from lattice peaks, correspond to an average over the entire probe depth of 130 nm. On the other hand, the satellite peak signal originates from the I* phase region, which is confined within the depth ξ_c below the sample's surface. Its actual position in reciprocal space depends on the a and c parameters averaged over the depth $\xi_c < 130$ nm, rather than on those presented in Figure 9. Despite this major limitation, the two conclusions given above about the dynamics of the I*-CDW wave vector hold:

(i) The a parameter averaged over a 130 nm depth decreases (Figure 9), which means that we may have underestimated the decrease of a over the depth ξ_c. In turn, we may have underestimated the averaged value of $a^* = 4\pi/a\sqrt{3}$ over the depth ξ_c, and thus

overestimated $q^{\parallel}_{I^*}/a^*$. Hence, our observation of a *shorter* I*-CDW wave vector with respect to the equilibrium value cannot be explained by this experimental artefact.

(ii) The orientation of the $\vec{a}^*$ and $\vec{b}^*$ vectors remains unchanged at all delays across the 130 nm probe depth (see Section 3.2.1). There are thus no reasons to evoke a rotation of the reciprocal space vectors over the depth ξ_c. As a result, the rotation of $\vec{q}^{\parallel}_{I^*}$ with respect to $\vec{a}^*$ can neither be explained by the differing diffracting volumes of the satellite and lattice peaks.

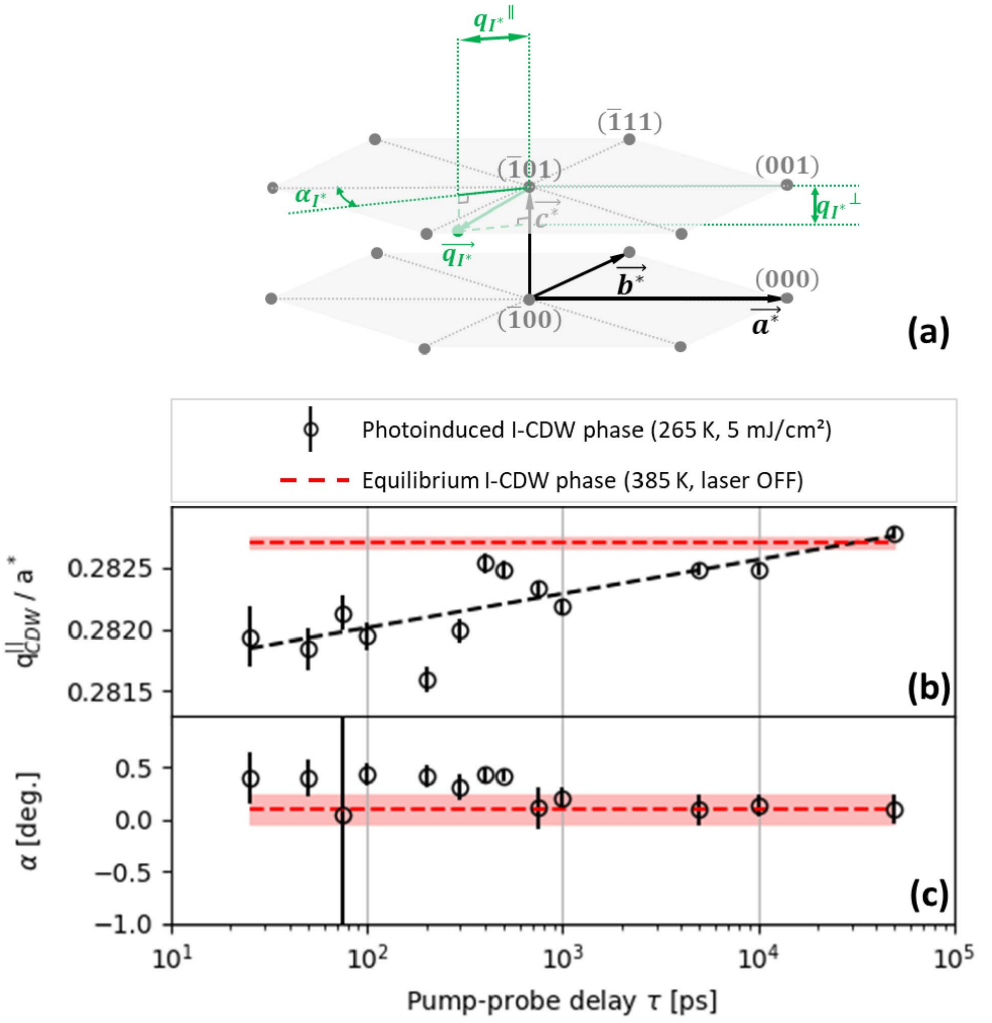

Figure 10. (a) Graphical definition of the I*-CDW wave vector components. (b,c) Time evolution of $\vec{q}^{\parallel}_{I^*}$ (black circles): (b) $\|\vec{q}^{\parallel}_{I^*}\|$ in a^* units, and (c) angle between $\vec{q}^{\parallel}_{I^*}$ and $-\vec{a}^*$, α_{I^*}. Values corresponding to the equilibrium I-CDW wave vector are also reported on panels (b,c), using red dashed lines. The error bars correspond to $\pm\sigma$ where σ is the standard deviation. Those were determined by propagating the errors on the $\varphi(\tau)$, $\delta(\tau)$ and $\gamma(\tau)$ angles of both the I* satellite peak and the $\bar{1}01$ lattice peak.

We emphasize that the observed dynamics of the I*-CDW wave vector cannot be attributed to a simple change of the average lattice temperature following laser excitation. Indeed, the wave vector of the I-CDW was shown to be temperature-independent in the range (350–420 K) [59,60]. For $\tau \leq 1$ ns, the I*-CDW thus *intrinsically* differs from the equilibrium I-CDW, not only by its limited correlation length, but also by its orientation and its larger periodicity in the $(\vec{a},\vec{b})$ plane ($q^{\parallel}_{I^*} < q^{\parallel}_{I}$). In equilibrium conditions, it is widely accepted that $\vec{q^{\parallel}_{I}}$ corresponds to a nesting vector of the 2D Fermi surface of 1T-TaS_2, lying close to one of the MK directions of reciprocal space [42, 62]. Given the local linear dispersion of the electronic state energies along the MK direction [63], a shorter nesting vector can be observed in the case where the Fermi energy is lowered consecutive to hole-doping. Shortening of the $\vec{q^{\parallel}_{I^*}}$ wave vector in 1T-TaS_2 has already been observed in chemically hole-doped samples [62]. As for the photoinduced I*-CDW phase, we propose that hole-doping is achieved in the pump–probe delay range $\tau \leq 30$ ns, owing to the presence of CDW dislocations. We further develop this idea in the following discussion. Understanding the larger value of α_{I^*} as compared to α_I is certainly a more complex task. The 1°-wide range of α_I reported in different samples of 1T-TaS_2 at equilibrium suggest that defects may play a role on the actual orientation of the I-CDW. A possibility would be that the CDW dislocations mentioned above influences the I*-CDW orientation.

4. Discussion

In the following, we first expose a detailed description of the mechanism of the photoinduced NC → I phase transition in 1T-TaS_2, based on past electron and X-ray diffraction studies. Considering the sequence of nucleation, growth, coalescence and phase ordering processes, we discuss the appearance of two kinds of topological defects, namely extended domain walls and dislocations. Their influence on the phase ordering kinetics as well as on the CDW period in the photoinduced I*-CDW phase of 1T-TaS_2 is finally examined in light of the present experimental results.

4.1. *Nucleation and growth of I*-CDW phase regions*

The development of the I*-CDW phase starts by the formation of several nuclei that subsequently grow [30]. Assuming that the I*-CDW phase regions are free from defects, their size limits the I*-CDW correlations lengths (Figure 6a) and one can write: $V_{I^*} \propto {\xi_{a,b}}^2 \times \xi_c$. Such a situation was evidenced in Ref. [33], where both V_{I^*} and the correlation lengths $\xi_{a,b}$ and ξ_c could be determined simultaneously, as in the present study. Since the I*-CDW period is incommensurate with that of the underlying lattice, there is an infinite number of energetically equivalent I*-CDW states, each corresponding to a distinct set of CDW phases $\theta^j_{I^*}$ ($j = 1,2,3$) [43]. Hence, in the early step of the photoinduced I*-CDW phase development, one can reasonably assume that isolated, defect-free I*-CDW phase regions appear, each being characterized by a distinct set of CDW phases.

4.2. *Coalescence*

At some point in the growth process of the isolated I*-CDW regions, coalescence is expected to occur. In a simple scenario, one can propose that the isolated I*-CDW regions then become CDW-phase domains in a single extended I*-CDW phase region, as sketched in Figures 6b and 11. Interestingly, the presence of CDW-phase domains was demonstrated experimentally in the equilibrium I-CDW phase, in freshly synthesized 1T-TaS_2 samples [64]. It was interpreted as resulting from the rapid quench performed at the end of the synthesis in order to avoid the formation of 2H-TaS_2 [39]. Ultrafast laser excitation and temperature quench, which both induce a sudden

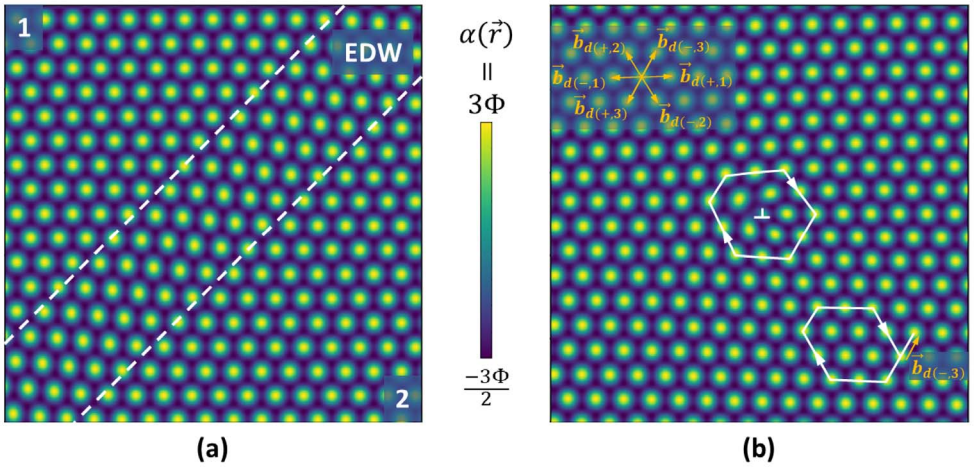

Figure 11. Spatial dependence of the I-CDW order parameter $\alpha(\vec{r})$ in a layer of 1T-TaS_2. (a) An extended domain wall (EDW) separates region 1 where the CDW-phases are $\theta_I^1 = \theta_I^2 = \theta_I^3 = 0$, and region 2 where $\theta_I^1 = -\pi$, $\theta_I^2 = \pi$ and $\theta_I^3 = 0$. (b) A dislocation is marked by the symbol $\perp$. Building the Burgers circuits around the dislocation and in a dislocation-free zone allows one to determine the Burgers vector of the dislocation, $\vec{b}_{d(-,3)}$. The 6 possible Burgers vectors of a I-CDW dislocation are depicted in the upper left part of the figure.

change of the atomic potential, are indeed expected to give rise to similar distributions of the CDW-phases $\theta_{I^*}^j(\vec{r})$. Let us note that the variation of the CDW-phases $\theta_{I^*}^j$ across CDW-phase domain boundaries causes an increase of the total internal energy that scales with the CDW-phase gradients squared [43]. As a consequence, the I*-CDW-phase domains are more likely separated by extended domain walls (Figure 11a) than by the sharp domains walls represented in Figure 6b, extended domains walls allowing a reduction of the CDW-phase gradients.

In addition to the elastic deformations of the I*-CDW described above, edge dislocations are susceptible to form in the CDW hexagonal lattice [43]. In analogy with edge dislocations in atomic lattices, it is expected that their Burgers vectors $\vec{b}_d$ link a maximum of the charge density with one of its six nearest neighbours, yielding 6 possibilities (Figure 11b): $\vec{b}_d(\pm, j) = \pm 2\pi / \| \vec{q}_{I^*}^{\parallel} \| \times \vec{q}_{I^*}^{\parallel j}$ ($j = 1,2,3$). Such dislocations were indeed found to appear in a time-dependent Ginzburg–Landau simulation of the formation of the I*-CDW [34]. This simulation showed that dislocations have already been formed 20 ps after laser excitation. However, the results available make it difficult to discuss whether the dislocations are created during coalescence of individual I*-CDW phase regions after a nucleation-growth process, or by another source of strain on the I*-CDW. In a scenario where dislocations are created during coalescence of defect-free I*-CDW phase regions in 1T-TaS_2, their Burgers vectors are expected to depend both on the orientation of the interfaces and on the CDW-phase differences between the regions. The possible configurations are in this case infinite, yielding a random distribution of each of the 6 types of dislocations.

4.3. *Phase ordering*

4.3.1. *Models for phase ordering*

Both extended domain walls and edge dislocations can evolve in time to let the correlation length increase (so-called phase-ordering processes).

When extended domain walls are present, the free energy is lowered by a reduction of the total domain wall area, through coarsening of the domain pattern. In this case, the average domain size (or I*-CDW correlation length) obeys a power-law scaling to time, following the Allen–Cahn growth law $\xi_{I^*} \propto \tau^{0.5}$ suitable for systems with non-conserved order parameters [65].

As mentioned previously, edge dislocations may also be present and limit the correlation length ξ_{I^*}. In this case, phase-ordering proceeds through a reduction of their total number, via pair annihilation of dislocations with opposite Burgers vectors. This process is driven by an attractive elastic interaction force with $1/r$ dependence (Peach–Koehler force) [66]. The problem of defect–antidefect pair annihilation has been studied theoretically in isotropic two-dimensional media where randomly distributed dislocations with $\vec{b}_d$ and $-\vec{b}_d$ Burgers vectors are present [67]. The surface density of defects is shown to decrease with a τ^{-1} behaviour. The correlation length ξ, defined as the average distance between two defects, then increases following $\tau^{0.5}$. In the case of a layer of 1T-TaS_2 the situation is more complex, as three types of defect-antidefect pairs coexist: $\vec{b}_{d(+,j)}$ and $\vec{b}_{d(-,j)}$ with $j = 1,2,3$. Dislocations with Burgers vectors $\vec{b}_{d(\pm,j)}$ and $\vec{b}_{d(\pm,j')}$ $(j' \neq j)$ are susceptible to interact elastically without being annihilated, which gives a *diffusive character* to their motions. In a diffusive motion regime and two-dimensional space, the surface density of randomly distributed defects is shown to decrease following a $\tau^{-0.5}$ power law [68]: correlation lengths then increase with a $\tau^{0.25}$ behaviour.

Both extended domain walls and edge dislocations are expected to be present in the photoinduced I*-CDW phase of 1T-TaS_2, each type of defect evolving according to its own dynamics. The growth kinetics of the CDW-phase domains is thus susceptible to strongly depend on the relative numbers of both types of defects. According to the above-mentioned models, domain coarsening following a τ^p power law is likely to be observed, with $0.25 \leq p \leq 0.5$. However, it is not excluded that the p exponent evolves with time, if the relative proportions of extended domain walls and edge dislocations change as a consequence of their distinct dynamics.

4.3.2. *Phase ordering as observed in the photoinduced I*-CDW phase*

The phase ordering process corresponds to an increase of the correlation length in a single region where the order parameter has already reached its equilibrium value. It thus translates into a coarsening of the domain pattern. In CDW systems, experimental evidence for phase ordering requires simultaneous measurement and analysis of the intensity and width of a CDW satellite peak. To our knowledge, coarsening of the CDW-phase domains was unambiguously observed only in the present work and in Ref. [32]. The data presented in this work show that, in the (25 ps–50 ns) range of pump–probe delays studied, the photoinduced I*-CDW phase undergoes phase-ordering in the $(\vec{a},\vec{b})$ plane with a $\tau^{0.22(4)}$ length-scaling. In Ref. [32], the I*-CDW phase was found to undergo phase-ordering in the $(\vec{a},\vec{b})$ plane with a $\tau^{0.5}$ length-scaling in the (100–500 ps) pump–probe delay range. Both experiments reveal domain coarsening, with correlation lengths increasing according to power laws in time τ^p. While the p exponents both fall in the range predicted by theoretical models, those differ significantly from one experiment to the other.

These markedly different behaviours might originate from the different excitation wavelengths and absorbed fluences used in Ref. [32] (1550 nm, 6.9 mJ/cm^2) and in the present work (800 nm, 3.9 mJ/cm^2), which results in differing depth-dependent profiles of absorbed energy density and, in turn, in differing profiles of quasi-equilibrium temperature once the excitation energy is transferred to the lattice after few picoseconds. Recalling that the growth kinetics of nucleated regions depends on temperature [69], one could propose that at the time of coalescence, the relative speeds of the I*-CDW phase fronts strongly differ in both experiments. This, in turn, could yield different distributions of extended domain walls and CDW-dislocations in the short-range correlated I*-CDW state, thereby influencing the coarsening dynamics.

Note that in the thick samples used for X-ray diffraction studies, the I*-CDW develops only close to the surface owing to the limited penetration depth of either the 800 nm or the 1550 nm photons of the pump pulse. Growth in the c-axis direction might be hindered by the small excitation depth, with possible repercussions on the growth or coarsening in the $(\vec{a},\vec{b})$ plane. In this respect, another explanation for the observation of the distinct coarsening dynamics following 800 nm (this work) and 1550 nm excitations (Ref. [32]) could stem from the differing excitation depths δ_L of 800 nm and 1550 nm photons, which amount 30 nm and 45 nm respectively.

Overall, the results presented in this work and Ref. [32] indicate that the kinetics of domain coarsening might depend on several parameters including the type of defects created in the I*-CDW and their distribution, as well as the limited extent of the I*-CDW in the c-axis direction. Determining the exact role of each of those parameters in the kinetics of phase ordering calls for additional experiments in thin samples (10 nm), using various excitation wavelengths and laser fluences.

4.3.3. *CDW dislocations and self-doping in the photoinduced I*-CDW phase*

Edge dislocations in CDWs are characterized by a local cancellation of the CDW-amplitude and a dipolar charge distribution associated with the π CDW-phase shift [66], which yields bound electronic states with energies distributed just below the Fermi energy (intra-CDW-gap states) [70]. Electrons trapped in those states do not belong to the CDW condensate, tantamount to a self-hole-doping in presence of CDW edge dislocations. The transient shortening of $q^{\parallel}_{I^*}$, which we attributed to a transient hole-doping of the photoinduced I*-CDW in Section 3.2.2, thus likely originates from the presence of dislocations in the I*-CDW phase. As coarsening occurs, the number of dislocations progressively decreases through pair-annihilation, thereby reducing the density of states of the intra-CDW-gap trapping sites. This, in turn, would explain the regular increase of $q^{\parallel}_{I^*}$ in the pump–probe delay range (25 ps–50 ns), towards its equilibrium value. It is interesting to note that in the experiment of Ref. [33], where the growth of isolated and *defect-free* I*-CDW regions was observed over an extended delay range (50 ps–10 ns), no significant changes of $q^{\parallel}_{I^*}$ could be detected despite a q-resolution comparable to the present experiment. This further supports the idea that the dynamics of $q^{\parallel}_{I^*}$ observed in the present work is related to the time-evolution of defects of the I*-CDW, in the form of I*-CDW dislocation annihilations.

The proportion of trapped electrons in the photoinduced I*-CDW phase can be inferred from the $q^{\parallel}_{I}$ dependence observed in chemically hole-doped samples. In 1T-$(Ta_{1-x}Ti_x)S_2$ for instance, Ta-atoms bring one conduction electron each, while Ti-atoms do not bring any: x then represents the fraction of holes among conduction electrons. Wilson *et al.* determined that $q^{\parallel}_{I}(x) = q^{\parallel}_{I}(x=0) \times [1 - 0.5327x]$ for $x \leq 0.25$ [62]. In 1T-TaS_2 at $\tau = 25$ ps, when the I*-CDW wave vector exhibits its smallest length, the ratio $q^{\parallel}_{I^*}/q^{\parallel}_{I}$ amounts 0.9969 (Figure 10b). This translates into a fraction $x_t(\tau = 25\text{ ps}) = 0.58\%$ of trapped electrons among conduction electrons or, equivalently, a surface density of trapped electrons $\rho_t(\tau = 25\text{ ps}) = (x_t(\tau = 25\text{ ps}))/(a^2 \times \sin(120)) = 5.9 \times 10^{-2}$ nm^{-2}. The average number of trapped electrons per dislocation can also be estimated. The I*-CDW correlation length in the $(\vec{a},\vec{b})$ plane allows calculating the surface density of dislocations: $\rho_d(\tau = 25\text{ ps}) = 4/\pi\xi^2_{a,b} = 1.4 \times 10^{-3}$ nm^{-2}. It follows that about 40 electrons would be trapped at each dislocation site.

Putting together the elements given in Section 3.2.2 and above, the complete scenario would be the following. The photoinduced I*-CDW phase differs from the I-CDW phase observed at equilibrium by the presence of topological defects, namely extended domain walls and CDW dislocations, which are formed at the time of coalescence of the nucleated I*-CDW phase regions. The dipolar charge distributions associated with CDW dislocations trap a fraction of the conduction electrons into intra-CDW-gap states, which lowers the Fermi energy and shrinks the

Fermi surface. The I-CDW modulation, which is driven by nesting of the Fermi surface, then exhibits a shorter wave vector $\vec{q}^{\parallel}_{I^*}$ as compared to the equilibrium I-CDW phase. As for the dynamics, the correlation lengths of the I*-CDW phase progressively increase on the ns timescale, owing to, among others, CDW dislocation annihilations. This causes a reduction of the density of intra-CDW-gap states and, in turn, an increase of the Fermi energy towards its equilibrium value. Concomitantly, the Fermi surface expands and the nesting vector $\vec{q}^{\parallel}_{I^*}$ elongates as shown in Figure 10b.

5. Summarizing conclusion and outlook

Based on the results of the present experiment and those of Refs. [32, 33], we built an improved description of the mechanisms at work behind the photoinduced NC → I phase transition in 1T-TaS_2. The photoinduced I*-CDW phase appears in the form of nuclei which subsequently grow. At this stage, the I*-CDW correlation lengths were shown to be limited by the size of the isolated I*-CDW regions [33], which highlights the absence of defects within those. The incommensurate nature of the I*-CDW enables an infinite number of energetically equivalent possibilities to position the charge density maxima relative to the underlying atomic lattice. Each isolated I*-CDW region is thus characterized by a distinct set of CDW-phases $(\theta^1_{I^*}, \theta^2_{I^*}, \theta^3_{I^*})$. When coalescence occurs, a single I*-CDW phase region emerges. It is fragmented into CDW-phase domains, reminiscent of the isolated I*-CDW regions with distinct CDW-phases. At this stage, the I*-CDW correlation length corresponds to the average distance between defects in the charge density modulation. CDW-phase accommodations between two adjacent domains can be achieved by two types of defects: extended domain walls and CDW-dislocations. Domain wall motions and dislocation annihilations allow the correlation lengths to increase, in a so-called phase-ordering process. In this regime, a self-similar growth of the CDW-phase domain pattern is observed with τ^p length-scaling (this work and Ref. [32]). p-exponents in the range (0.22–0.5) can be retrieved from the available experimental data, which compares reasonably well with the results of existing theories on coarsening [65, 67, 68].

In the present work, we have shown that the photoinduced I*-CDW phase differs from the I-CDW phase at equilibrium, not only by its limited correlation length, but also by a larger period of the CDW modulation (shorter wave vector of the CDW). We propose that the increased period of the I*-CDW modulation would be due to a smaller number of conduction electrons involved in the collective CDW state, some of them being trapped at CDW-dislocation sites. In this view, the I*-CDW appears as a hole-doped I-CDW.

This and previous works [32] indicate that the kinetics of phase ordering in the photoinduced I*-CDW phase could be influenced by the distribution of extended domain walls and CDW-dislocations. The latter distribution arises from complex interactions between nucleated regions at the time of coalescence, which likely depend on the quasi-equilibrium temperature reached once the laser pulse energy is transferred to the lattice. The next challenge will certainly consist in achieving a complete description of defect formation in the photoinduced I*-CDW. In this view, performing wavelength-dependent studies at short timescales, when coalescence of the initially formed I*-CDW regions occurs, would be of high interest.

Acknowledgements

We wish to warmly thank Philippe Hollander (SOLEIL synchrotron) for his continuous efforts toward improving laser operation at CRISTAL beamline, as well as Frédéric Picca (SOLEIL synchrotron) for his precious help at the time of integrating functionalities of the GHKL library into our analysis scripts. We acknowledge SOLEIL for provision of synchrotron radiation at CRISTAL beamline (proposal number 20171529).

References

[1] E. Dagotto, "Correlated electrons in high-temperature superconductors", *Rev. Mod. Phys.* **66** (1994), p. 763-840.

[2] M. Imada, A. Fujimori, Y. Tokura, "Metal–insulator transitions", *Rev. Mod. Phys.* **70** (1998), p. 1039-1263.

[3] K. Nasu, *Photoinduced Phase Transitions*, World Scientific Publishing, Singapore, 2004.

[4] K. Yonemitsu, K. Nasu, "Theory of photoinduced phase transitions in itinerant electron systems", *Phys. Rep.* **465** (2008), p. 1-60.

[5] J. Zhang, R. D. Averitt, "Dynamics and control in complex transition metal oxides", *Annu. Rev. Mater. Res.* **44** (2014), p. 19-43.

[6] D. N. Basov, R. D. Averitt, D. Hsieh, "Towards properties on demand in quantum materials", *Nat. Mater.* **16** (2017), p. 1077-1088.

[7] E. Janod, J. Tranchant, B. Corraze, M. Querre, P. Stoliar, M. Rozenberg, T. Cren, D. Roditchev, V. T. Phuoc, M.-P. Besland, L. Cario, "Resistive switching in mott insulators and correlated systems", *Adv. Funct. Mater.* **25** (2015), p. 6287-6305.

[8] A. Singer, S. K. K. Patel, R. Kukreja, V. Uhlíř, J. Wingert, S. Festersen, D. Zhu, J. M. Glownia, H. T. Lemke, S. Nelson, M. Kozina, K. Rossnagel, M. Bauer, B. M. Murphy, O. M. Magnussen, E. E. Fullerton, O. G. Shpyrko, "Photoinduced enhancement of the charge density wave amplitude", *Phys. Rev. Lett.* **117** (2016), article no. 056401.

[9] V. L. R. Jacques, C. Laulhé, N. Moisan, S. Ravy, D. L. Bolloc'h, "Laser-induced charge-density-wave transient depinning in chromium", *Phys. Rev. Lett.* **117** (2016), article no. 156401.

[10] P. Stoliar, J. Tranchant, B. Corraze, E. Janod, M.-P. Besland, F. Tesler, M. Rozenberg, L. Cario, "A leaky-integrate-and-fire neuron analog realized with a mott insulator", *Adv. Funct. Mater.* **27** (2017), article no. 1604740.

[11] C. Adda, B. Corraze, P. Stoliar, P. Diener, J. Tranchant, A. Filatre-Furcate, M. Fourmigué, D. Lorcy, M.-P. Besland, E. Janod, L. Cario, "Mott insulators: a large class of materials for leaky integrate and fire (LIF) artificial neuron", *J. Appl. Phys.* **124** (2018), article no. 152124.

[12] G. Grüner, *Density Waves in Solids*, Perseus Publishing, Cambridge, MA, 2000.

[13] F. Schmitt, P. Kirchmann, U. Bovensiepen, R. Moore, L. Rettig, M. Krenz, J.-H. Chu, N. Ru, L. Perfetti, D. Lu, M. Wolf, I. Fisher, Z.-X. Shen, "Transient electronic structure and melting of a charge density wave in $TbTe_3$", *Science* **321** (2008), p. 1649-1652.

[14] A. Tomeljak, H. Schäfer, D. Städter, M. Beyer, K. Biljakovic, J. Demsar, "Dynamics of photoinduced charge-density-wave to metal phase transition in $K_{0.3}MoO_3$", *Phys. Rev. Lett.* **102** (2009), article no. 066404.

[15] R. Yusupov, T. Mertelj, V. V. Kabanov, S. Brazovskii, P. Kusar, J.-H. Chu, I. R. Fisher, D. Mihailovic, "Coherent dynamics of macroscopic electronic order through a symmetry-breaking transition", *Nat. Phys.* **6** (2010), p. 681-684.

[16] M. Eichberger, H. Schäfer, M. Krumova, M. Beyer, J. Demsar, H. Berger, G. Moriena, G. Sciaini, R. J. D. Miller, "Snapshots of cooperative atomic motions in the optical suppression of charge density waves", *Nature* **468** (2010), p. 799-802.

[17] S. Hellmann, M. Beye, C. Sohrt, T. Rohwer, F. Sorgenfrei, H. Redlin, M. Kallaäne, M. Marczynski-Bühlow, F. Hennies, M. Bauer, A. Föhlisch, L. Kipp, W. Wurth, K. Rossnagel, "Ultrafast melting of a charge-density wave in the mott insulator 1T-TaS_2", *Phys. Rev. Lett.* **105** (2010), article no. 187401.

[18] T. Rohwer, S. Hellmann, M. Wiesenmayer, C. Sohrt, A. Stange, B. Slomski, A. Carr, Y. Liu, L. Avila, M. Kalläne, S. Mathias, L. Kipp, K. Rossnagel, M. Bauer, "Collapse of long-range charge order tracked by time-resolved photoemission at high momenta", *Nature* **471** (2011), p. 490-493.

[19] E. Möhr-Vorobeva, S. L. Johnson, P. Beaud, U. Staub, R. Desouza, C. Milne, G. Ingold, J. Demsar, H. Schaefer, A. Titov, "Nonthermal melting of a charge density wave in $TiSe_2$", *Phys. Rev. Lett.* **107** (2011), article no. 036403.

[20] S. Hellmann, T. Rohwer, M. Kalläne, K. Hanff, C. Sohrt, A. Stange, A. Carr, M. Murnane, H. Kapteyn, L. Kipp, M. Bauer, K. Rossnagel, "Time-domain classification of charge-density-wave insulators", *Nat. Commun.* **3** (2012), article no. 1069.

[21] T.-R. T. Han, Z. Tao, S. D. Mahanti, K. Chang, C.-Y. Ruan, C. D. Malliakas, M. G. Kanatzidis, "Structural dynamics of two-dimensional charge-density waves in $CeTe_3$ investigated by ultrafast electron crystallography", *Phys. Rev. B* **86** (2012), article no. 075145.

[22] N. Erasmus, M. Eichberger, K. Haupt, I. Boshoff, G. Kassier, R. Birmurske, H. Berger, J. Demsar, H. Schwoerer, "Ultrafast dynamics of charge density waves in $4H_b$–$TaSe_2$ probed by femtosecond electron diffraction", *Phys. Rev. Lett.* **109** (2012), article no. 167402.

[23] P. Zhu, J. Cao, Y. Zhu, J. Geck, Y. Hidaka, S. Pjerov, T. Ritschel, H. Berger, Y. Shen, R. Tobey, J. P. Hill, X. J. Wang, "Dynamic separation of electron excitation and lattice heating during the photoinduced melting of the periodic lattice distortion in 2H-$TaSe_2$", *Appl. Phys. Lett.* **103** (2013), article no. 071914.

[24] T. Huber, S. O. Mariager, A. Ferrer, H. Schäfer, J. A. Johnson, S. Grübel, A. Lübcke, L. Huber, T. Kubacka, C. Dornes, C. Laulhé, S. Ravy, G. Ingold, P. Beaud, J. Demsar, S. L. Johnson, "Coherent structural dynamics of a prototypical charge-density-wave-to-metal transition", *Phys. Rev. Lett.* **113** (2014), article no. 026401.

[25] A. Zong, A. Kogar, Y.-Q. Bie, T. Rohwer, C. Lee, E. Baldini, E. Ergeçen, M. B. Yilmaz, B. Freelon, E. J. Sie, H. Zhou,

J. Straquadine, P. Walmsley, P. E. Dolgirev, A. V. Rozhkov, I. R. Fisher, P. Jarillo-Herrero, B. V. Fine, N. Gedik, "Evidence for topological defects in a photoinduced phase transition", *Nat. Phys.* **15** (2019), p. 27-31.

[26] A. Zong, P. E. Dolgirev, A. Kogar, E. Ergeçen, M. B. Yilmaz, Y.-Q. Bie, T. Rohwer, I.-C. Tung, J. Straquadine, X. Wang, Y. Yang, X. Shen, R. Li, J. Yang, S. Park, M. C. Hoffmann, B. K. Ofori-Okai, M. E. Kozina, H. Wen, X. Wang, I. R. Fisher, P. Jarillo-Herrero, N. Gedik, "Dynamical slowing-down in an ultrafast photoinduced phase transition", *Phys. Rev. Lett.* **123** (2019), article no. 097601.

[27] M. Trigo, P. Giraldo-Gallo, M. E. Kozina, T. Henighan, M. P. Jiang, H. Liu, J. N. Clark, M. Chollet, J. M. Glownia, D. Zhu, T. Katayama, D. Leuenberger, P. S. Kirchmann, I. R. Fisher, Z. X. Shen, D. A. Reis, "Coherent order parameter dynamics in $SmTe_3$", *Phys. Rev. B* **99** (2019), article no. 104111.

[28] S. Sun, L. Wei, Z. Li, G. Cao, Y. Liu, W. J. Lu, Y. P. Sun, H. Tian, H. Yang, J. Li, "Direct observation of an optically induced charge density wave transition in 1T-$TaSe_2$", *Phys. Rev. B* **92** (2015), article no. 224303.

[29] T.-R. T. Han, F. Zhou, C. D. Malliakas, P. M. Duxbury, S. D. Mahanti, M. G. Kanatzidis, C.-Y. Ruan, "Exploration of metastability and hidden phases in correlated electron crystals visualized by femtosecond optical doping and electron crystallography", *Sci. Adv.* **1** (2015), article no. e1400173.

[30] K. Haupt, M. Eichberger, N. Erasmus, A. Rohwer, J. Demsar, K. Rossnagel, H. Schwoerer, "Ultrafast metamorphosis of a complex charge-density wave", *Phys. Rev. Lett.* **116** (2016), article no. 016402.

[31] L. L. Guyader, T. Chase, A. H. Reid, R. K. Li, D. Svetin, X. Shen, T. Vecchione, X. J. Wang, D. Mihailovic, H. A. Dürr, "Stacking order dynamics in the quasi-two-dimensional dichalcogenide 1T-TaS_2 probed with mev ultrafast electron diffraction", *Struct. Dyn.* **4** (2017), article no. 044020.

[32] C. Laulhé, T. Huber, G. Lantz, A. Ferrer, S. O. Mariager, S. Grübel, J. Rittmann, J. A. Johnson, V. Esposito, A. Lübcke, L. Huber, M. Kubli, M. Savoini, V. L. R. Jacques, L. Cario, B. Corraze, E. Janod, G. Ingold, P. Beaud, S. L. Johnson, S. Ravy, "Ultrafast formation of a charge density wave state in 1T-TaS_2: observation at nanometer scales using time-resolved X-ray diffraction", *Phys. Rev. Lett.* **118** (2017), article no. 247401.

[33] G. Lantz, C. Laulhé, S. Ravy, M. Kubli, M. Savoini, K. Tasca, E. Abreu, V. Esposito, M. Porer, A. Ciavardini, L. Cario, J. Rittmann, P. Beaud, S. L. Johnson, "Domain-size effects on the dynamics of a charge density wave in 1T-TaS_2", *Phys. Rev. B* **96** (2017), article no. 224101.

[34] S. Vogelgesang, G. Storeck, J. G. Horstmann, T. Diekmann, M. Sivis, S. Schramm, K. Rossnagel, S. Schäfer, C. Ropers, "Phase ordering of charge density waves traced by ultrafast low-energy electron diffraction", *Nat. Phys.* **14** (2018), p. 184-190.

[35] L. Stojchevska, I. Vaskivskyi, T. Mertelj, P. Kusar, D. Svetin, S. Brazovskii, D. Mihailovic, "Ultrafast switching to a stable hidden quantum state in an electronic crystal", *Science* **344** (2014), p. 177-180.

[36] Y. A. Gerasimenko, P. Karpov, I. Vaskivskyi, S. Brazovskii, D. Mihailovic, "Intertwined chiral charge orders and topological stabilization of the light-induced state of a prototypical transition metal dichalcogenide", *NPJ Quantum Mater.* **4** (2019), article no. 32.

[37] A. Kogar, A. Zong, P. E. Dolgirev, X. Shen, J. Straquadine, Y.-Q. Bie, X. Wang, T. Rohwer, I.-C. Tung, Y. Yang, R. Li, J. Yang, S. Weathersby, S. Park, M. E. Kozina, E. J. Sie, H. Wen, P. Jarillo-Herrero, I. R. Fisher, X. Wang, N. Gedik, "Light-induced charge density wave in $LaTe_3$", *Nat. Phys.* **16** (2019), p. 159-163.

[38] D. Mihailovic, "The importance of topological defects in photoexcited phase transitions including memory applications", *Appl. Sci.* **9** (2019), article no. 890.

[39] J. A. Wilson, F. J. di Salvo, S. Mahajan, "Charge-density waves and superlattices in the metallic layered transition metal dichalcogenides", *Adv. Phys.* **24** (1975), p. 117-201.

[40] T. Ishiguro, H. Sato, "Electron microscopy of phase transformations in 1T-TaS_2", *Phys. Rev. B* **44** (1991), no. 5, p. 2046-2060.

[41] A. Spijkerman, J. L. de Boer, A. Meetsma, G. A. Wiegers, S. van Smaalen, "X-ray crystal-structure refinement of the nearly commensurate phase of 1T-TaS_2 in (3 + 2)-dimensional superspace", *Phys. Rev. B* **56** (1997), no. 21, p. 13757-13767.

[42] K. Rossnagel, "On the origin of charge-density waves in selected layered transition-metal dichalcogenides", *J. Phys. Condens. Matter* **23** (2011), article no. 213001.

[43] W. L. McMillan, "Landau theory of charge-density waves in transition-metal dichalcogenides", *Phys. Rev. B* **12** (1975), p. 1187-1196.

[44] K. Momma, F. Izumi, "Vesta 3 for three-dimensional visualization of crystal, volumetric and morphology data", *J. Appl. Crystallogr.* **44** (2011), p. 1272-1276.

[45] S. Ravy, C. Laulhé, J. P. Itié, P. Fertey, B. Corraze, S. Salmon, L. Cario, "High-pressure X-ray diffraction study of 1T-TaS_2", *Physica B* **407** (2012), p. 1704-1706.

[46] A. Beal, H. Hughes, W. Liang, "The reflectivity spectra of some group va transition metal dichalcogenides", *J. Phys., C, Solid State Phys.* **8** (1975), p. 4236-4248.

[47] M.-A. Tordeux, J. Barros, A. Bence, P. Brunelle, N. Hubert, M. Labat, A. Nadji, L. Nadolski, P. Lebasque, J.-P. Pollina, C. Evain, "Low-alpha operation for the soleil storage ring", in *Proceedings of the 2012 International Particle Accelerator Conference (IPAC12)*, JACoW - Joint Accelerator Conferences Website, Geneva, 2012, p. 1608-1610.

[48] B. Henke, E. Gullikson, J. Davis, "X-ray interactions: photoabsorption, scattering, transmission, and reflection at e = 50–30000 eV, z = 1–92", *At. Data Nucl. Data Tables* **54** (1993), p. 181-342.
[49] K. Medjoubi, S. Hustache, F. E. Picca, J. Bérar, N. Boudet, F. Bompard, P. Breugnon, J.-C. Clémens, A. Dawiec, P. Delpierre, B. Dinkenspiler, S. Godiot, J.-P. Logier, M. Menouni, C. Morel, M. Nicolas, P. Pangaud, E. Vigeolas, "Performance and applications of the CdTe- and Si-XPAD3 photon counting 2D detector", *J. Instrum.* **6** (2011), article no. C01080.
[50] J.-P. Ricaud, P. Betinelli-Deck, J. Bisou, X. Elattaoui, C. Laulhé, P. Monteiro, L. S. Nadolski, G. Renaud, S. Ravy, M. Silly, F. Sirotti, "The timbel synchronization board for time-resolved experiments at synchrotron soleil", in *Proceedings of the 2011 International Conference on Accelerator and Large Experimental Physics Control Systems (ICALEPCS2011)*, JACoW - Joint Accelerator Conferences Website, Geneva, 2011, p. 1036-1038.
[51] L. Perfetti, P. A. Loukakos, M. Lisowski, U. Bovensiepen, H. Berger, S. Biermann, P. S. Cornaglia, A. Georges, M. Wolf, "Time evolution of the electronic structure of 1T-TaS_2 through the insulator–metal transition", *Phys. Rev. Lett.* **97** (2006), article no. 067402.
[52] L. Perfetti, P. A. Loukakos, M. Lisowski, U. Bovensiepen, M. Wolf, H. Berger, S. Biermann, A. Georges, "Femtosecond dynamics of electronic states in the mott insulator 1T-TaS_2 by time resolved photoelectron spectroscopy", *New J. Phys.* **10** (2008), article no. 053019.
[53] L. Rettig, R. Cortés, J.-H. Chu, I. R. Fisher, F. Schmitt, R. G. Moore, Z.-X. Shen, P. S. Kirchmann, M. Wolf, U. Bovensiepen, "Persistent order due to transiently enhanced nesting in an electronically excited charge density wave", *Nat. Commun.* **7** (2016), article no. 10459.
[54] P. Monceau, "Electronic crystals: an experimental overview", *Adv. Phys.* **61** (2012), p. 325-581.
[55] F. E. Picca, Ghkl's documentation [https://people.debian.org/~picca/hkl/hkl.html], Université Paris-Saclay (Synchrotron SOLEIL), 91190, Saint-Aubin, France.
[56] C. Thomsen, H. T. Grahn, H. J. Maris, J. Tauc, "Surface generation and detection of phonons by picosecond light pulses", *Phys. Rev. B* **34** (1986), p. 4129-4138.
[57] S. Lee, G. J. Williams, M. I. Campana, D. A. Walko, E. C. Landahl, "Picosecond X-ray strain rosette reveals direct laser excitation of coherent transverse acoustic phonons", *Sci. Rep.* **6** (2016), article no. 19140.
[58] K. Motizuki (ed.), *Structural Phase Transitions in Layered Transition Metal Compounds*, Springer, Netherlands, 1986.
[59] C. B. Scruby, P. M. Williams, G. S. Parry, "The role of charge density waves in structural transformations of 1T-TaS_2", *Philos. Mag.* **31** (1975), p. 255-274.
[60] K. Nakanishi, H. Takatera, Y. Yamada, H. Shiba, "The nearly commensurate phase and effect of harmonics on the successive phase transitions in 1T-TaS_2", *J. Phys. Soc. Japan* **43** (1977), p. 1509-1517.
[61] J. van Landuyt, G. van Tendeloo, S. Amelinckx, "Electron diffraction study of inter- and intrapolytypic phase transition in transition metal dichalcogenides. III. complementary diffraction studies and lattice imaging of the deformation waves", *Phys. Status Solidi A* **36** (1976), p. 757-777.
[62] J. A. Wilson, F. J. di Salvo, S. Mahajan, "Charge-density waves in metallic, layered, transition-metal dichalcogenides", *Phys. Rev. Lett.* **32** (1974), p. 882-885.
[63] L. F. Mattheiss, "Band structures of transition-metal-dichalcogenide layer compounds", *Phys. Rev. B* **8** (1973), p. 3719-3740.
[64] J.-D. Su, A. R. Sandy, J. Mohanty, O. G. Shpyrko, M. Sutton, "Collective pinning dynamics of charge-density waves in 1T-TaS_2", *Phys. Rev. B* **86** (2012), article no. 205105.
[65] A. J. Bray, "Theory of phase-ordering kinetics", *Adv. Phys.* **51** (2002), p. 481-587.
[66] D. Feinberg, J. Friedel, "Elastic and plastic deformations of charge density waves", *J. Phys. (France)* **49** (1988), p. 485-496.
[67] H. Toyoki, "Pair annihilation of pointlike topological defects in the ordering process of quenched systems", *Phys. Rev. A* **42** (1990), p. 911-917.
[68] D. Toussaint, F. Wilczek, "Particle-antiparticle annihilation in diffusive motion", *J. Chem. Phys.* **78** (1983), p. 2642-2647.
[69] P. Papon, J. Leblond, P. H. E. Meijer, *The Physics of Phase Transitions: Concepts and Applications*, Springer, Netherlands, 2006.
[70] K. Maki, X. Z. Huang, "Phase vortices in charge-density-wave conductors", *Phys. Rev. B* **37** (1988), p. 8668-8673.